



# Enhanced UV–Visible photocatalytic activity of Cu-doped ZnO/TiO<sub>2</sub> nanoparticles

Mohammad Reza Delsouz Khaki<sup>1</sup> · Mohammad Saleh Shafeeyan<sup>2</sup> · Abdul Aziz Abdul Raman<sup>1</sup> · Wan Mohd Ashri Wan Daud<sup>1</sup>

Received: 25 November 2017 / Accepted: 29 December 2017 / Published online: 1 February 2018  
© Springer Science+Business Media, LLC, part of Springer Nature 2018

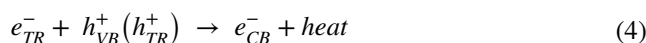
## Abstract

Cu–ZnO/TiO<sub>2</sub> nanoparticles were prepared by entrapping copper ions into crystalline matrix of ZnO/TiO<sub>2</sub> through sol–gel synthesis method. The photocatalyst matrix loaded with different copper concentrations was calcined at 500 and 700 °C. Thermal property, crystalline structure, surface morphology and absorption spectra of Cu–ZnO/TiO<sub>2</sub> were characterized by thermogravimetric analysis, X-ray diffraction, scanning electron microscopy, transmission electron microscope and UV–Vis spectrophotometry. Besides, its specific surface area and band gap energy level were estimated through BET surface area method, Kubelka–Munk model and Planck’s equation. The results revealed that Cu–ZnO/TiO<sub>2</sub> had a more thermally stable lattice compared to TiO<sub>2</sub>/ZnO and hence the phase transformation from anatase to rutile is retarded under higher calcination temperature in Cu–ZnO/TiO<sub>2</sub> lattice. The photoactivity of Cu–ZnO/TiO<sub>2</sub> was then evaluated through degradation of methyl orange under visible light irradiation. Among different samples, the samples that were calcined at 500 °C exhibited the highest photocatalytic activity compared to those calcined at 700 °C. Cu–ZnO/TiO<sub>2</sub> with a Cu content of 3 wt% was observed to have the maximum activity, giving C/C<sub>0</sub> value of 0.03 after 150 min. This value was about 12 and 28.3 times higher than that of ZnO/TiO<sub>2</sub> and TiO<sub>2</sub>, respectively.

## 1 Introduction

Titanium dioxide (TiO<sub>2</sub>), an n-type semiconductor, is one of the most applicable photo-catalysts which can be used for a wide range of applications such as H<sub>2</sub> generation, self-cleaning, defogger, water purification, air purification, sterilization and etc [1–7]. TiO<sub>2</sub> is non-toxic, abundant, economical, versatile and stable [8–10]. Generally, TiO<sub>2</sub> is a semiconductor with a wide band gap and it requires an excitation light with a wavelength lower than 400 nm ( $E_g = hc/\lambda \cong 1240/\lambda$ ) to begin a photo-reaction [11, 12]. When surface of TiO<sub>2</sub> (or any other photo-catalyst) is irradiated with UV light irradiation, electrons ( $e_{CB}^-$ ) and holes ( $h_{VB}^+$ ) are created in conduction (CB) and valence bands (VB), respectively [13]. The generated electrons and holes

are subsequently trapped and recombined with each other. In short, the photo-induced formation procedure follows four steps, which are photo-excitation (Eq. 1) charge-carrier trapping of  $e^-$  (Eq. 2), charge-carrier trapping of  $h^+$  (Eq. 3) and electron–hole recombination (Eq. 4):



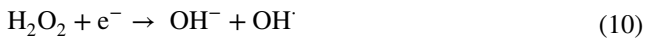
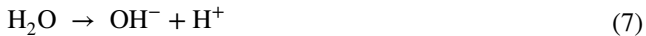
In the next step, the photo-induced electrons in the CB are trapped by aqueous adsorbed oxygen and participate in the reduction processes, producing superoxide radical anions ( $O_2^-$ ) (Eq. 5). The superoxides are protonated (Eq. 6) by  $H^+$  which is produced by ionization of water at the generated holes ( $h^+$ ) (Eq. 7). ( $HOO^{\cdot}$ ) then traps another excited electron to produce  $HO_2^-$  (Eq. 8), followed by protonation of  $HO_2^-$  to generate hydrogen peroxide, as shown in Eq. 9. Finally, hydrogen peroxide is decomposed to produce hydroxyl radicals ( $OH^{\cdot}$ ) (Eq. 10). Meanwhile, the photo-induced holes in the VB diffuse to the surface of the photo-catalyst and then

✉ Mohammad Saleh Shafeeyan  
ms.shafeeyan@gmail.com

<sup>1</sup> Department of Chemical Engineering, Faculty of Engineering, University of Malaya, 50603 Kuala Lumpur, Malaysia

<sup>2</sup> Department of Engineering and Technology, Golestan University, Aliabad Katool, Iran

react with the adsorbed water molecules, generating another hydroxyl radical (Eq. 11) [14–17].



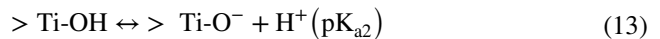
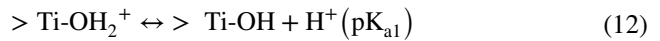
A variety of organisms, organic and inorganic pollutants can be deactivated, decomposed or transformed by the synergistic interaction of hydroxyl radicals, electrons, holes and other oxidating radicals [18, 19].

In  $\text{TiO}_2$  photo-catalyst, the CB energy level is slightly higher than the reduction potential of oxygen ( $E_{\text{CB}} = -0.51$  V,  $E_{\text{O}} = -0.33$  V) which is a predominant electron acceptor (or oxidant) and it can ease the transfer of  $e^-_{\text{CB}}$  to  $\text{O}_2$ . On the other hand, its VB energy level ( $E_{\text{VB}} = +2.69$  V) is much lower than the oxidation potentials of most electron donors (either organic or inorganic compounds). Accordingly, the highly oxidative holes can be transferred to the surface-adsorbed hydroxide groups or water by devising the surface-bound hydroxyl radical [20]. Generally, it can be concluded that  $\text{TiO}_2$  encourages redox transformation of pollutants due to the positions of its bands.

In addition,  $\text{TiO}_2$  has three main crystalline structures; anatase (tetragonal), rutile (tetragonal) and brookite (orthorhombic). Anatase is the phase normally fabricated in the sol-gel process but brookite is mostly found as a by-product when precipitation is performed in an acidic medium at low temperature. Rutile is a stable structure while both brookite and anatase are metastable and usually transfigured to rutile when heated. Generally, brookite is more reactive than anatase. However, preparing pure brookite without rutile or anatase is rather difficult and therefore it has not been widely investigated [21]. Besides, anatase has a higher photocatalytic activity compared to rutile because its higher  $E_{\text{CB}}$  ( $\sim 0.2$  eV) results in higher driving force for transferring electron to  $\text{O}_2$ . It is because  $E_{\text{CB}}$  position affects electron transfer rate and subsequently, charge recombination rate. Therefore, it is a determining factor for efficiency of photocatalysis. It has always been reported that the photocatalytic activities of both anatase and rutile structures are highly influenced by the types of substrates applied [22–25].

Surface properties of  $\text{TiO}_2$ , particularly the pH dependence of the surface charge, are the other determinants for

photocatalytic reaction.  $\text{TiO}_2$  is known to be diprotic acid due to the amphoteric nature of the surface hydroxyl groups. Accordingly, the surface titanol group of this photocatalyst follows the below acid–base equilibrium reaction:



The averaged  $\text{pK}_{\text{a}}$ , is defined as the pH of zero point of charge ( $\text{pH}_{\text{zpc}}$ ), at which the surface charge of photocatalyst is null. For  $\text{TiO}_2$  photocatalyst,  $\text{pK}_{\text{a1}} = 4.5$ ,  $\text{pK}_{\text{a2}} = 8$  and the  $\text{pH}_{\text{zpc}}$  value is estimated to be 6.2 [26, 27]. Therefore, protonation reaction takes place and the catalyst surface is positively charged at  $\text{pH} < 6.2$ , while the catalyst surface is negatively charged at  $\text{pH} > 6.2$  due to deprotonation reaction.

Apart from the mentioned properties of  $\text{TiO}_2$ , this photocatalyst is highly reactive during the photocatalysis for water treatment and it has a great response even under weak light irradiation. However,  $\text{TiO}_2$  is inappropriate for a mass processing system and is inactive and inapplicable in visible light. Numerous efforts have been proposed aiming to overcome such limitations and enhance the photocatalytic activity of  $\text{TiO}_2$ , through surface modification/complexation, sensitization, impurity doping, hetero-junction with semiconductors of similar band gap, etc. The latter two were focused in this study.

In doping process, the fast charge recombination is retarded and visible light absorption is enabled by creating defect states in the band gap. In the first case, the recombination is inhibited and the interfacial charge transfer is enhanced by trapping the VB holes or CB electrons in the defect sites. In the second case, the electronic transitions from the defect states to the CB or from the VB to the defect states are allowed under sub-band gap irradiation. Metal ions (transition metals and noble metals) and non-metal ions are the two main categories of dopants [28, 29]. Generally, selective metals are preferred since they have the potential to transfer electron and decrease the band gap energy level [30–32]. For doped catalysts, metal ions are activated in the presence of light source, generating electron–holes. Therefore, the presence of metal ion dopants in the photocatalyst matrix improves the interfacial electron-transfer rates and charge carrier recombination rates significantly, followed by greater photoreactivity. Among different metallic doping elements, copper has been proven as an effective dopant to enhance visible light absorption. For example, Park et al. [33] modified  $\text{TiO}_2$  through  $\text{Ni}^{2+}$ ,  $\text{Co}^{2+}$ ,  $\text{Zn}^{2+}$ ,  $\text{Cu}^{2+}$  incorporations and reported that Cu-doped  $\text{TiO}_2$  was a promising photocatalyst in photo-decomposition of methylene blue. Sangpour et al. [34] modified  $\text{TiO}_2$  by doping it with Ag, Au, and Cu and found that doping increased the probability of radical formation. The level of photo-activity of the

investigated photocatalysts was reported to be in the following order:  $\text{Cu}:\text{TiO}_2 > \text{Au}:\text{TiO}_2 > \text{Ag}:\text{TiO}_2 > \text{TiO}_2$ .

On the other hand, in hetero-junction process, the synergic effects of two semiconductors with similar band gap can result in low recombination rate and increase the lifetime of the electron–hole pair. For  $\text{TiO}_2$  photocatalyst, it can potentially be coupled with the other semiconductors i.e.  $\text{SiO}_2$ ,  $\text{MoO}_3$ ,  $\text{CdS}$ ,  $\text{MgO}$ ,  $\text{WO}_3$ ,  $\text{SnO}_2$ ,  $\text{Cu}_2\text{O}$ ,  $\text{In}_2\text{O}_3$  and  $\text{ZnO}$  [35]. Among different semiconductors, the photocatalytic activity of  $\text{ZnO}$  is almost similar to  $\text{TiO}_2$  and found to be as reactive as  $\text{TiO}_2$  under sunlight. In other words, the band gap of  $\text{ZnO}$  (around 3.37 eV) is close to the energy level of titanium dioxide [36]. According to the literature, the energy level and surface area of  $\text{TiO}_2$  increase when it is mixed with another photocatalyst. Besides, the range of light absorption shifts towards visible light due to narrowing of band gap energy level as  $\text{TiO}_2$  is doped with a semiconductor catalyst [37].

$\text{TiO}_2/\text{ZnO}$  has been investigated by a number of researchers to improve the photodegradation efficiency of  $\text{TiO}_2$  catalyst [38, 39]. The ability of copper in modifying the photoactivity of  $\text{TiO}_2$  [40–42] and  $\text{ZnO}$  [43, 44] has been separately investigated in various works. Besides, the hybrid photocatalyst of  $\text{TiO}_2/\text{ZnO}$  with some other metals has also been investigated in some studies [45, 46]. However, to the best of our knowledge, the hybrid photocatalyst of  $\text{Cu-ZnO}/\text{TiO}_2$  has not been investigated yet. Accordingly, in the present work, the hetero-junction of  $\text{TiO}_2$  with  $\text{ZnO}$  with  $\text{Cu}$  integrated into the structure was investigated, aiming at narrowing the band gap energy of  $\text{TiO}_2$  and enhancing the hybrid photocatalyst's photoactivity under visible light irradiation.  $\text{Cu-ZnO}/\text{TiO}_2$  was fabricated through sol gel process and analysed in terms of thermal property, crystalline structure, surface morphology, specific surface area, wavelength absorption and band gap energy level. Finally, the photocatalytic activity of the synthesized catalyst was evaluated through methyl orange (MO) degradation under visible light.

## 2 Materials and methods

### 2.1 Materials

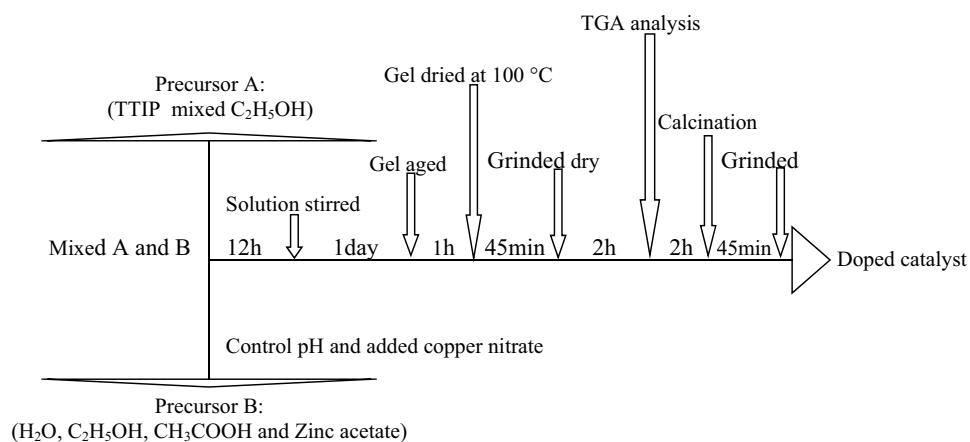
Titanium(IV) isopropoxide (TTIP,  $\text{Ti}[\text{OCH}(\text{CH}_3)_2]_4$ , 97%) used to synthesize titanium dioxide was purchased from Sigma Aldrich. Zinc acetate dihydrate ( $\text{Zn}(\text{CH}_3\text{COO})_2 \cdot 2\text{H}_2\text{O}$ , > 98%) and Copper(II) nitrate trihydrate ( $\text{Cu}(\text{NO}_3)_2 \cdot 3\text{H}_2\text{O}$ , 99%) were purchased from Chemical U.K. Acetic acid ( $\text{CH}_3\text{COOH}$ , 98%) and hydrochloric acid ( $\text{HCl}$ ,  $M = 36.45 \text{ g/mol}$ ) were also supplied by the same company. Ethanol ( $\text{C}_2\text{H}_5\text{OH}$  > 99.8%) and methyl orange (MO) were supplied by Merck.

### 2.2 Samples preparation

In the present study,  $\text{Cu-ZnO}/\text{TiO}_2$  was synthesized using sol–gel method [47, 48]. Figure 1 shows a simplified diagram of the synthesis. The process includes three main steps, which are gel preparation, drying and calcination.

In this study, the synthesis started with preparation of precursor A and B. For precursor A, a predetermined amount of TTIP was mixed with ethanol and stirred for an hour at room temperature to get a precursor solution. For precursor B, a predetermined amount of distilled water, ethanol, acetic acid and zinc acetate (according to the adequate weight ratio of  $\text{TiO}_2:\text{ZnO}$ ) were mixed together by continuous and tempestuous agitation. Meanwhile, the solution pH value was controlled between 2.0 and 3.0 by adding certain quantity of hydrochloric acid solution. Afterwards, a certain amount of copper(II) nitrate trihydrate was added to precursor B with vigorous stirring for metal doping. Then, precursor B was dropped into precursor A at a speed of one drop per second under strong stirring. The produced mixture was continuously stirred for about 12 h to complete the sol–gel process and a transparent sol was then created. It was aged for one day to

**Fig. 1** Diagram of  $\text{Cu-ZnO}/\text{TiO}_2$  synthesis process



finish the sol–gel transition and evaporate excess alcohol. After that, it was thermally-treated in an electric oven at 100 °C for 1 h. In the next step, the catalysts went through the calcination process which was carried out in a furnace (Thermconcept KL 15/11) with a heating rate of 10 °C/min to almost the maximum temperature determined by the TGA process. Calcination continued for 2 h to regulate the molecular network and structure of the photocatalyst and to remove excess solvent. It should be noted that heating process was conducted before calcination and the results were analysed in order to determine the thermal resistance of the synthesised samples and the calcination temperature. Moreover, 10 different samples with TiO<sub>2</sub> to ZnO weight ratio of 7:3 and Cu loadings of 1–5 wt% were generated. The samples were then calcined at two different temperatures (500 and 700 °C) and characterized subsequently. In order to evaluate and compare the photocatalytic activity of Cu–ZnO/TiO<sub>2</sub>, pure TiO<sub>2</sub> and ZnO/TiO<sub>2</sub> were also synthesized separately.

### 2.3 Characterization

Thermo-Gravimetric Analyser (TG-Q500, Research instrument, USA) was employed to analyse the thermal stability of the synthesized photocatalysts. Quantity of the synthesized catalysts was subjected to heating process starting from the room temperature to the maximum temperature of 1000 °C, under a dynamic nitrogen atmosphere. Identification of the structures and phase purity of Cu–ZnO/TiO<sub>2</sub> samples were carried out by an X-ray diffractometer (XRD) using an advanced X-ray diffraction (7602 EA Almelo, analytical Empyrean, Netherlands). A scanning rate of 0.026°s<sup>-1</sup> in 2θ ranging from 20° to 80° was used. Morphology studies of the samples were conducted using scanning electron microscope (SEM) (field emission scanning electron microscope, FEI Quanta, The Netherlands). It operated at a beam energy level of 10.00 kV under high vacuum level and spot size of 3.0. Transmission electron microscope (TEM) images were used to observe the internal structure of sample (ORIU SC1000). The microscope had accelerating voltage from 20 to 200 kV and standard magnification from ×22 to ×930K. The surface area of the samples was determined using Brunauer–Emmett–Teller (BET) surface area method (Micromeritics, tristar II 3020). The UV–Vis (diffuse reflectance) spectra in the wave length range of 200–800 nm was obtained using a spectrophotometer equipped with an integrated sphere (UV–Vis–NIR spectrophotometer Uv-3600, Shimadzu, Japan). Accordingly, the band gap energy level was determined through the Kubelka–Munk's model. The results were further compared with that estimated through Plank's equation.

### 2.4 Photocatalytic activity

The photocatalytic activity of the synthesized photocatalysts was evaluated through photocatalytic degradation of methyl orange (MO) solution as a test contaminant in aqueous solution under visible light irradiation [49]. The results were further compared to the photocatalytic ability of pure TiO<sub>2</sub>, and ZnO/TiO<sub>2</sub>.

The photocatalyst was suspended in methyl orange solution and the suspension was magnetically stirred in dark for 30 min to reach adsorption–desorption equilibrium prior to irradiation. Then, the suspension was irradiated by visible light at λ > 400 nm (100W, Soft White, Philips) for 150 min and the photocatalysis was monitored within this duration. At the same time, the suspension was maintained by bubbling air continuously during the reaction. All photocatalytic tests were conducted at ambient temperature (25 ± 1 °C) and the reaction vessel was surrounded by a water jacket to keep the temperature stable. The first sample of each experiment was taken after 15 min and the subsequent samples were taken every 30 min. The degradation percentage of MO was assessed using Eq. (14).

$$\alpha\% = [(C_0 - C_t) \times 100] / C_0 \quad (14)$$

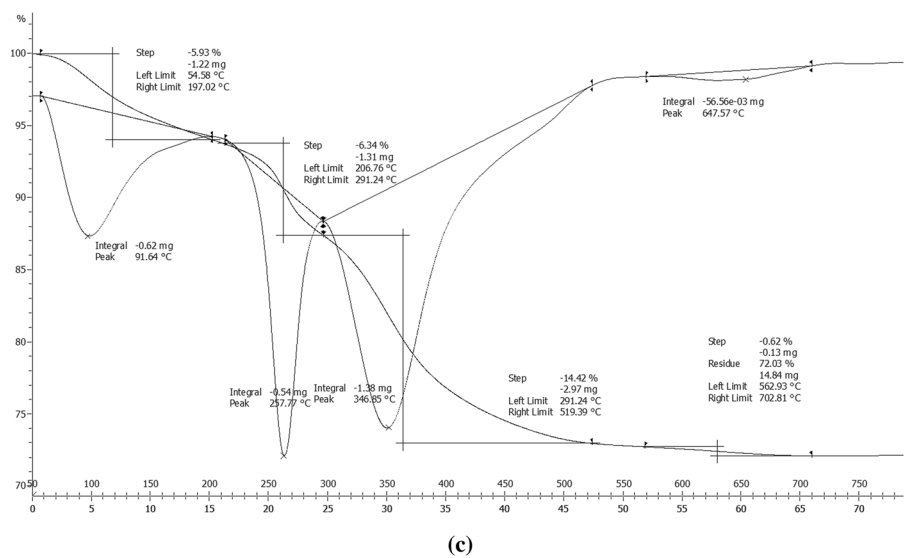
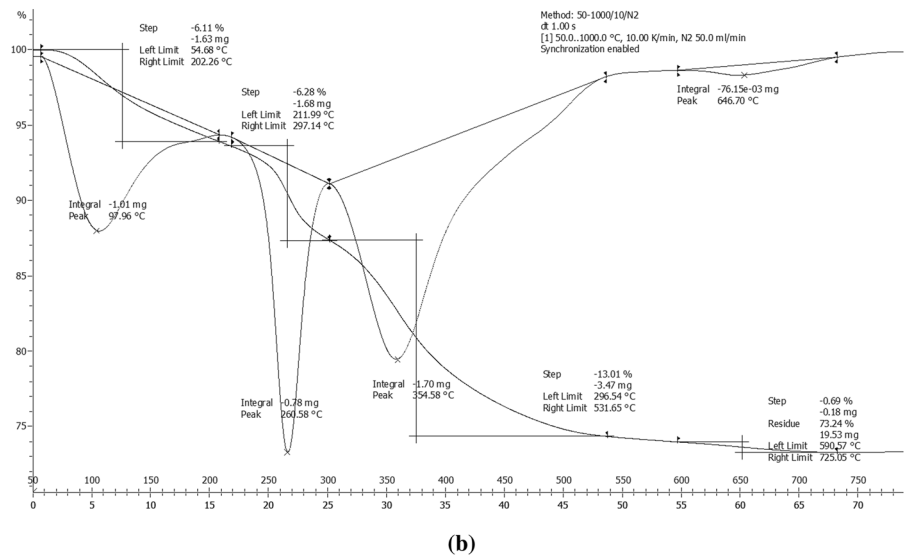
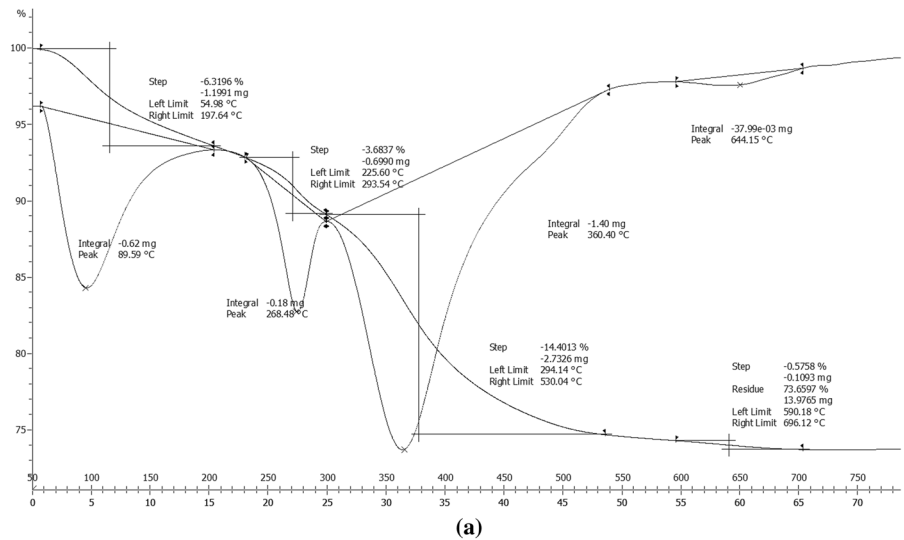
where, C<sub>0</sub> and C<sub>t</sub> denote initial and instantaneous concentrations of MO (mg L<sup>-1</sup>), respectively.

## 3 Results and discussion

### 3.1 Thermal stability of Cu–ZnO/TiO<sub>2</sub>

In order to clarify the thermal stability of the Cu–ZnO/TiO<sub>2</sub> composite powder, thermo-gravimetry analysis was conducted using the dried composite gel with Cu mass fraction of 1, 3 and 5 wt%. The results of weight loss due to decomposition and Derivative Thermogravimetric Analysis (DTG) are shown in Fig. 2. Three main phases of mass loss during the whole thermal decomposition/combustion process were identified. The minor weight loss of 5.93–6.31 wt%, as observed in all the graphs at the temperature below 115 °C, was due to the loss of physically adsorbed water and solvent [50]. This phase slightly decreased (around 1 wt%) as the Cu concentration increased. The decomposition phase started after solvent evaporation. Based on Fig. 2, this phase happened from 200 to 260 °C, resulting in a reduction of 3.68, 6.28 and 6.34 wt% in the total mass. As observed, the mass reduction was dramatically lower at copper concentration of 1 wt%. The third step, which occurred at about 270 to 380 °C, was related to both the decomposition of the organic group's residuals and the condensation of the TiO<sub>2</sub> anatase phases. Similar results were also reported by

**Fig. 2** TGA curves of the Cu–ZnO/TiO<sub>2</sub> composite powder with Cu concentrations of solid lines Cu (0 wt%), dotted lines Cu (1 wt%), dashed dotted Cu (5 wt%). (heating speed of 10 °C/min)





Ramimoghdam et al. [51]. From the analysis, the temperature assigned for this phase shifted to lower range with increasing Cu caused by compounds created by copper. Such results demonstrated the influence of copper and its corresponding compounds on the thermal stability of Cu–ZnO/TiO<sub>2</sub>.

### 3.2 Structural characterizations of Cu–ZnO/TiO<sub>2</sub>

In addition, TiO<sub>2</sub> has three main crystalline structures; anatase (tetragonal), rutile (tetragonal) and brookite (orthorhombic). Anatase is the phase normally fabricated in the sol–gel process but brookite is mostly found as a by-product when precipitation is performed in an acidic medium at low temperature. Rutile is a stable structure while both brookite and anatase are metastable and usually transfigured to rutile when heated. Generally, brookite is more reactive than anatase. However, preparing pure brookite without rutile or anatase is rather difficult and therefore it has not been widely investigated [21]. Besides, anatase has a higher photocatalytic activity compared to rutile because its higher E<sub>CB</sub> (~ 0.2 eV) results in higher driving force for transferring electron to O<sub>2</sub>. It is because E<sub>CB</sub> position affects electron transfer rate and subsequently, charge recombination rate. Therefore, it is a determining factor for efficiency of photocatalysis. It has always been reported that the photocatalytic activities of both anatase and rutile structures are highly influenced by the types of substrates applied [22–25].

X-ray diffraction (XRD) clarifies the crystal structures of Cu–ZnO/TiO<sub>2</sub> in different TiO<sub>2</sub> and ZnO concentrations and calcination temperatures. Figure 3a and b displays the XRD patterns of the samples containing 1–5 wt% Cu, calcined at 500 °C (Fig. 3a) and 700 °C (Fig. 3b), respectively. The standard JCPDS patterns of Zinc Oxide (reference code 98-002-9272), crystal phases of TiO<sub>2</sub> including Anatase (00-021-1272), Rutile (01-075-1750) and Brookite (00-029-1360), Cu<sub>2</sub>O (00-05-0667) and CuO (00-48-1548) were used to analyse the obtained patterns in this study.

Generally, for Cu–ZnO/TiO<sub>2</sub> with copper loading of 1 wt% which was calcined at 500 °C, the crystal was rather amorphous. However, it crystallized well as the copper content increased in the matrix. Besides, as shown in Fig. 3a and Table 1, among TiO<sub>2</sub> crystal structures, diffraction peaks of anatase and brookite showed the strongest intensities after calcination at 500 °C, indicating their major phases within the photocatalyst at this stage. Meanwhile, traces of rutile were also detected in Cu–ZnO/TiO<sub>2</sub> calcined at 500 °C. As the calcination temperature rose to 700 °C, the crystalline phases changed accordingly. The strongest peaks in these samples were neither from brookite nor anatase, but rutile, indicating a crystal phase transfer towards rutile at the temperature of 700 °C. These observations are in good agreement with those obtained in the literature [52]. As reported

by Paola et al. [21], anatase structure was normally generated in TiO<sub>2</sub> synthesis through sol–gel method whereas brookite was normally found as a by-product when the precipitation was performed in an acidic medium at low temperature. Rutile is the stable structure while brookite and anatase are metastable and can potentially transform to rutile when heated.

Besides TiO<sub>2</sub> crystals, ZnO with strong diffraction peak intensities were found in these photocatalysts. However, a number of ZnO peaks on the basis of standard peaks were not identifiable in this study. Meanwhile, more ZnTiO<sub>3</sub> were clearly detected, especially for those calcined at 700 °C, indicating an extensive reaction, Eq. (15) [55].



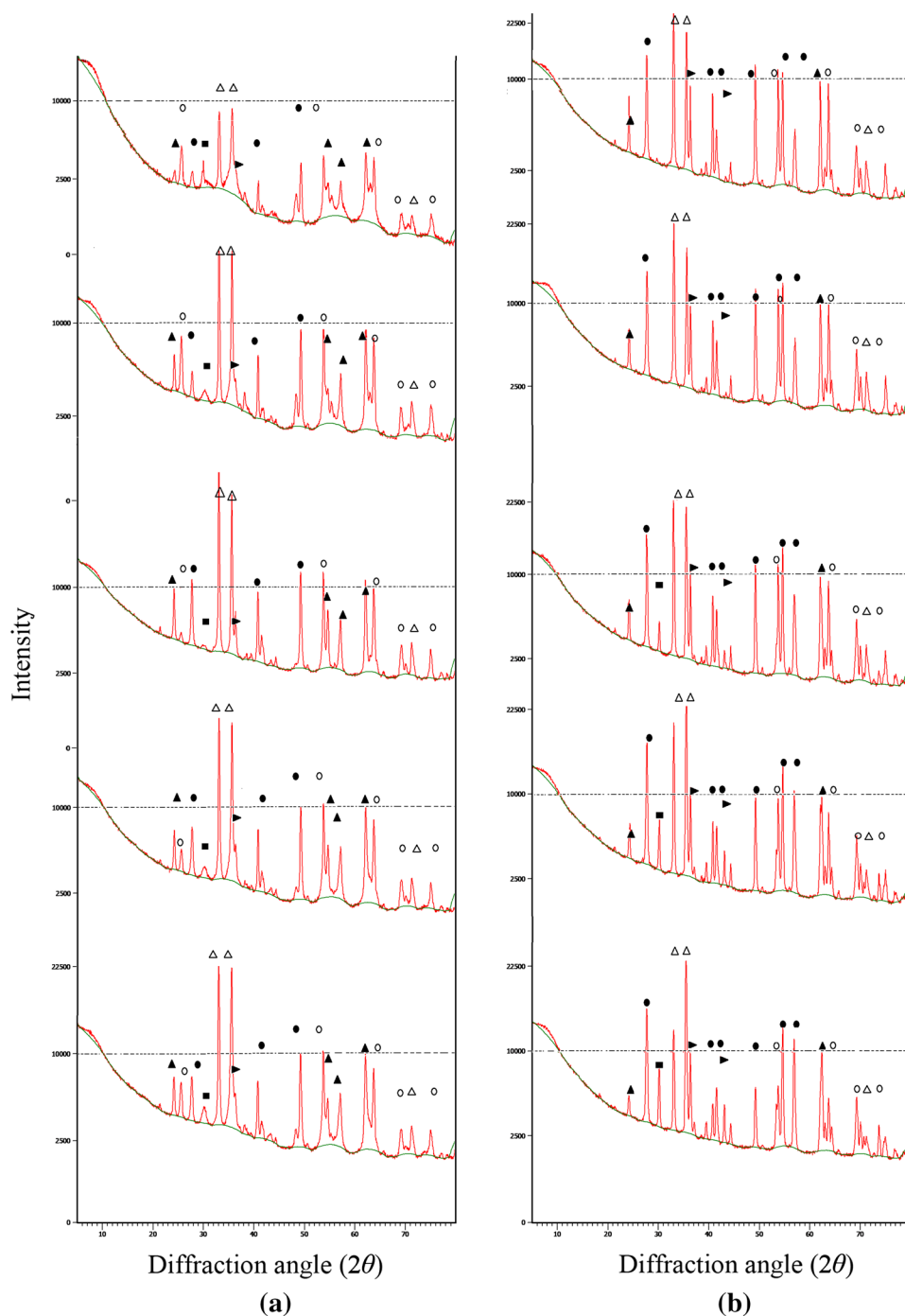
The results confirmed that photodeposition modified the basic crystal structure of ZnO and transformed it into ZnTiO<sub>3</sub> or ZnTiO<sub>4</sub>. The phenomena may be due to the homogeneous dispersion of nanoscale copper deposits on the surface of ZnO. On the other hand, presence of high quantity of zincite in samples calcined at 500 °C indicated that the aforementioned transformation was not fully achieved for photocatalysis at that temperature.

In terms of copper quantity, according to the XRD patterns (Fig. 3) and Table 1, signals of Cu<sub>2</sub>O were clearly observed ( $2\theta$  of about 29.63°) and the intensity of these peaks increased with copper loading, which clarified that higher mass fraction of Cu<sub>2</sub>O was obtained with copper loading. Whereas, the diffraction pattern of CuO was not observed as CuO or small dimensions of Cu components were below the detection limit of XRD. The other possible reason might be high dispersion of CuO within the TiO<sub>2</sub> frameworks.

Furthermore, by comparing the XRD patterns of Cu–ZnO/TiO<sub>2</sub> with that of pure TiO<sub>2</sub> [56] and considering the Cu content in both the photocatalysts calcined at 500 and 700 °C, it was found that the anatase phase increased initially with the Cu content up to 2 wt% and beyond that, the percentage of the anatase phase slightly reduced.

Meanwhile, the quantity of rutile phase was reinforced in both categories of the synthesised Cu–TiO<sub>2</sub>/ZnO. Accordingly, it can be suggested that the dopant content beyond 2 %wt promoted the phase transformation from anatase to rutile. The reason was that the surface oxygen vacancy concentration of anatase grains is enhanced with Cu, rearranging the ions favourably and reorganizing the structure into the rutile structure [57]. In other words, since the synthesised photocatalysts were calcined at atmospheric condition, the chemical state of Cu is Cu<sup>+</sup> (on the basis of XRD pattern) which can be a substitute to Ti<sup>4+</sup> transformed TiO<sub>2</sub> into a denser rutile phase. The other possible reason was that the density of surface defects of the photocatalyst may increase as Cu content increased, resulting in phase transformation

**Fig. 3** XRD patterns of synthesized Cu–ZnO/TiO<sub>2</sub> calcined at **a** 500 °C, **b** 700 °C. Open circle anatase, filled circle rutile, filled triangle brookite, open triangle ZnO, right pointed filled triangle ZnTiO<sub>3</sub>, filled square Cu<sub>2</sub>O, filled triangle Cu<sub>2</sub>HNO<sub>3</sub>



since the surface defects were considered as the rutile nucleation sites [58]. This finding was consistent with that of Fe-doped TiO<sub>2</sub> [59] or Al-doped TiO<sub>2</sub> [60]. Besides, anatase phase percentage in Cu–TiO<sub>2</sub>/ZnO reduced with increasing the calcination temperature from 500 to 700 °C, which is opposite of the trend passed by rutile phase in those calcination temperatures. Therefore, the rutile phase dominated the TiO<sub>2</sub> structure when the calcinating temperature was 700 °C (Fig. 3).

On the other hand, a number of anatase phase peaks appeared stable at both 500 and 700 °C. It was attributed to thermodynamic stability of anatase. High thermodynamic stability of anatase, compared to rutile phase, is a proven phenomenon in smaller crystallites [61–63]. But the effect of doping should also be considered. During the sol–gel process, dopant significantly controls the crystallite growth (especially for crystallization of anatase phase). Although the dopant content increased the rutile nucleation sites or

**Table 1** Crystallite size and surface area of the Cu–ZnO/TiO<sub>2</sub> photocatalyst prepared at various calcination temperatures and compound concentrations

Photocatalyst	Cu content (wt%)	Calcination temperature (°C)	Crystal size (nm)	Surface area (m <sup>2</sup> /g)	Ref
ZnO	–	500	33.0	–	[53]
ZnO	–	700	30.0	–	[53]
TiO <sub>2</sub>	–	500	18.9	–	[54]
TiO <sub>2</sub>	–	700	42.3	–	[54]
Cu–ZnO/TiO <sub>2</sub>	1	500	28.2	29.1	This study
Cu–ZnO/TiO <sub>2</sub>	2	500	37.1	–	This study
Cu–ZnO/TiO <sub>2</sub>	3	500	37.6	71.2	This study
Cu–ZnO/TiO <sub>2</sub>	4	500	38.2	–	This study
Cu–ZnO/TiO <sub>2</sub>	5	500	39.9	117.9	This study
Cu–ZnO/TiO <sub>2</sub>	1	700	36.1	37.4	This study
Cu–ZnO/TiO <sub>2</sub>	2	700	42.4	–	This study
Cu–ZnO/TiO <sub>2</sub>	3	700	50.8	80.1	This study
Cu–ZnO/TiO <sub>2</sub>	4	700	53.3	–	This study
Cu–ZnO/TiO <sub>2</sub>	5	700	54.9	126.6	This study

transferred TiO<sub>2</sub> into denser rutile, Cu<sub>2</sub>O and CuO molecules adsorbed on the surface of TiO<sub>2</sub> made crystal growth slow. Therefore, the key is the balance between the amount of dopant that behaves as the rutile nucleation sites and the amount of Cu<sub>2</sub>O or CuO which is adsorbed on the surface of the photo catalyst.

### 3.3 Crystal size and specific surface area of Cu–ZnO/TiO<sub>2</sub>

The average crystal size of nanoparticles were determined from the full-width of the half maximum (FWHM) of the most intense peaks of the respective crystals using the Scherrer's equation,  $D = C_s \cdot k/\beta \cdot \cos \theta$ , where  $D$  is equal to or smaller than the grain crystallite size,  $C_s$  is the Scherrer constant, which has a value between 0.9 and 1.2, depending on the shape of the particles (in this study,  $C_s=0.94$ ),  $k$  is the wave length of the incident X-ray,  $\theta$  is the Bragg diffraction angle and  $\beta$  is the full-width of the half maximum [64]. Accordingly, TiO<sub>2</sub> peaks of (105) (211) (204) for anatase phase, TiO<sub>2</sub> peaks of (110) (211) (220) for rutile phase and TiO<sub>2</sub> peaks of (320) (151) (052) for Brookite phase, ZnO

peaks of (002), (101) and ZnTiO<sub>3</sub> peak of (103) were considered. However, brookite peaks of (320) (151) were only considered for calcination temperatures of 500 °C while rutile peaks of (211) (220) were only considered for calcination temperatures of 700 °C. The specific surface area of the synthesized photocatalysts was also estimated through Brunauer–Emmett–Teller (BET) surface area method [65, 66]. The results are presented in Table 1.

Generally, the mean crystallite size of Cu–ZnO/TiO<sub>2</sub> was highly influenced by calcination temperature. As observed, when calcination temperature rose from 500 to 700 °C, the crystal size of Cu–ZnO/TiO<sub>2</sub> increased gradually. It was mainly attributed to phase transformation from anatase to rutile and ZnO–ZnTiO<sub>3</sub>. In other words, the increase in calcination temperature induced phase transformation and accelerated the growth of crystallites. Increase of crystal size with calcination temperature has also been reported by many other researchers [61, 67–70]. The XRD patterns showed that the most intense anatase peak with the width of (101) plane at  $2\theta = 25.6$  appeared at calcination temperature of 500 °C and disappeared by increasing the calcination temperature to almost 700 °C. The XRD patterns also showed that the rutile phase peaks became broader and more intense at 700 °C (i.e. (200) plane at  $2\theta = 39.5$ , (111) plane at  $2\theta = 41.5$ , (210) plane at  $2\theta = 43$ , etc). To get a quantitative view, at 500 °C the crystallite size of rutile phase reached a maximum of 35.04 nm, but it became 39.93 nm as the temperature increased to 700 °C at a copper concentration of 5 wt%. At the same condition, the crystallite size of ZnO dropped from 33.17 to 28.73 nm. Meanwhile, ZnTiO<sub>3</sub> monotonically increased from 30.99 to 34.08 nm with calcination temperature, showing the transformation of ZnO to ZnTiO<sub>3</sub> through Eq. 15. From Table 1, it was observed that the average crystal size increased with dopant loading, which was attributed to phase transformation and in agreement with other published works. For example, Inturi et al. [71] who investigated the effect of different dopants on TiO<sub>2</sub> crystals reported that, Ce, Y, Zr and Mo reduced anatase crystal size while other metals, i.e. V, Cr, Fe, Co, Mn, Ni and Cu increased crystal size.

The specific surface areas of the synthesized Cu–ZnO/TiO<sub>2</sub> along with pure ZnO and TiO<sub>2</sub> are also listed in Table 1. From the table, it was noted that all Cu–ZnO/TiO<sub>2</sub> photocatalysts possessed a remarkably higher surface area than pure ZnO and TiO<sub>2</sub>, thus demonstrating higher ability to photoexcite the electron–hole pairs in the active sites and causing stronger absorption of reactants on the catalyst surface [72]. However, as observed, the specific surface area for the synthesized photocatalyst was sacrificed as the dopant content or calcination temperature increased. Decrease in surface area by increasing the amount of copper doped with TiO<sub>2</sub> was also reported by [73]. In other words, the slight increase in crystal size led to a small decrease in the surface



area on the Cu-doped photocatalysts. Therefore, the maximum crystal size along with the minimum surface area was observed in the samples with the Cu amount of 5 wt%, calcined at 700 °C. It can be suggested different concentrations of Cu led to certain degree of stability of the specific surface area of Cu-doped photocatalysts.

### 3.4 Morphology of Cu–ZnO/TiO<sub>2</sub>

Morphologies of the Cu–ZnO/TiO<sub>2</sub> photocatalyst were investigated by SEM and the results are shown in Figs. 4 and 5. Figure 4 shows the photocatalyst morphology as its copper doping increased (1, 2 and 5 wt%) whereas the effect of calcination temperature is demonstrated in Fig. 5.

As discussed earlier (in the XRD analysis), the photocatalyst with 1.0 wt% Cu synthesized at 500 °C mainly comprised amorphous crystals. That observation was also confirmed by the SEM image in Fig. 4a. As observed, the surface of the catalyst was smooth and crash free. Furthermore, according to the XRD analysis, the dopant concentration played a dominant role by either behaving as the rutile nucleation sites or being adsorbed on the surface of the photo catalyst. The SEM images also showed that the crystalline lattice improved by increasing the dopant content in the matrix of the photocatalyst matrix (Fig. 4b). Figure 4c shows that the crystallinity was extended and improved notably as the dopant increased to 5 wt%.

Apart from the effects of the dopant content, the crystallinity became more regular as the calcination temperature increased to 700 °C, as shown in Fig. 5a and b. This result was also in line with that obtained by the XRD analysis. At this condition, Cu–ZnO/TiO<sub>2</sub> contained approximately 100% of specific monodisperse abundant dumbbell or ball shaped particles and nano-pores. As observed, calcination temperature favourably affected the growth of nanophase crystals due to crystal phase transformation. For better analysis, the TEM images of Cu (3 wt%)–TiO<sub>2</sub>/ZnO calcined at 500 and 700 °C are presented in Fig. 6. Figure 6a and c show a typical agglomeration of the powder proving the tendency of Cu ions to form the complex with the surface oxygen of TiO<sub>2</sub> and ZnO. As per images, the particles in the samples with dopant content of 3 wt% calcined at either 500 or 700 °C, have distributed uniformly. Figure of 6b also depicts that the Cu–TiO<sub>2</sub>/ZnO consists of a large number of particulates with a size of around 30–40 nm which is consistent with the results of XRD. Both single and accumulated particles were clearly observed in Fig. 6b. Corresponding results for the photocatalyst synthesized at 700 °C were also presented in Fig. 6d. In contrast, the samples calcined at 700 °C showed a slight larger particle size than that calcined at lower temperature, which is in agreement with the results obtained by XRD. Furthermore, it is observed that by increasing the

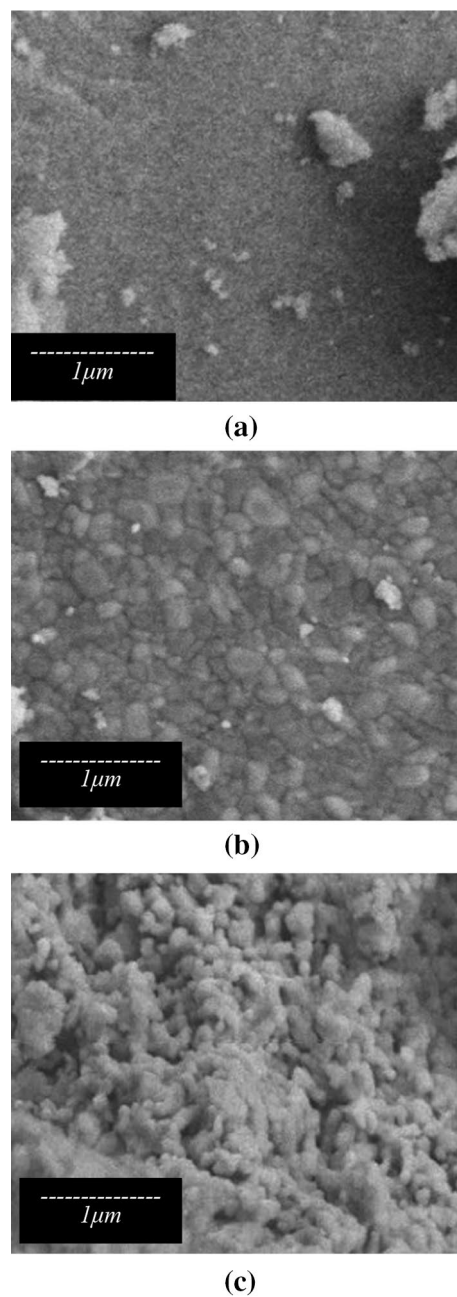


**Fig. 4** SEM images of Cu–ZnO/TiO<sub>2</sub>, **a** Cu=1 wt%, calcined at 500 °C, **b** Cu=5 wt%, calcined at 500 °C, **c** Cu=1 wt%, calcined at 700 °C, **d** Cu=5 wt%, calcined at 700 °C

calcination temperature, crystallinity have increased too, however, the impact of dopant should not be eliminated.

### 3.5 Analysis of optical absorption of Cu–ZnO/TiO<sub>2</sub>

The analysis of UV–Vis diffuse reflectance spectra (converted to absorbance) for Cu–ZnO/TiO<sub>2</sub> with different Cu content, calcined at 500 and 700 °C are shown in Fig. 7. Generally, incorporation of copper into TiO<sub>2</sub>/ZnO lattice

**Fig. 5** SEM images of Cu–ZnO/TiO<sub>2</sub>, **a** Cu = 5 wt%, calcined at 500 °C, **b** calcined at 700 °C

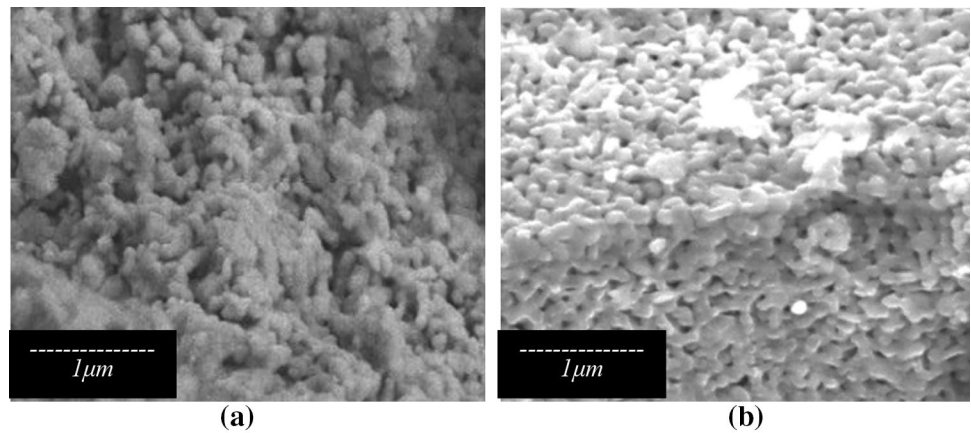
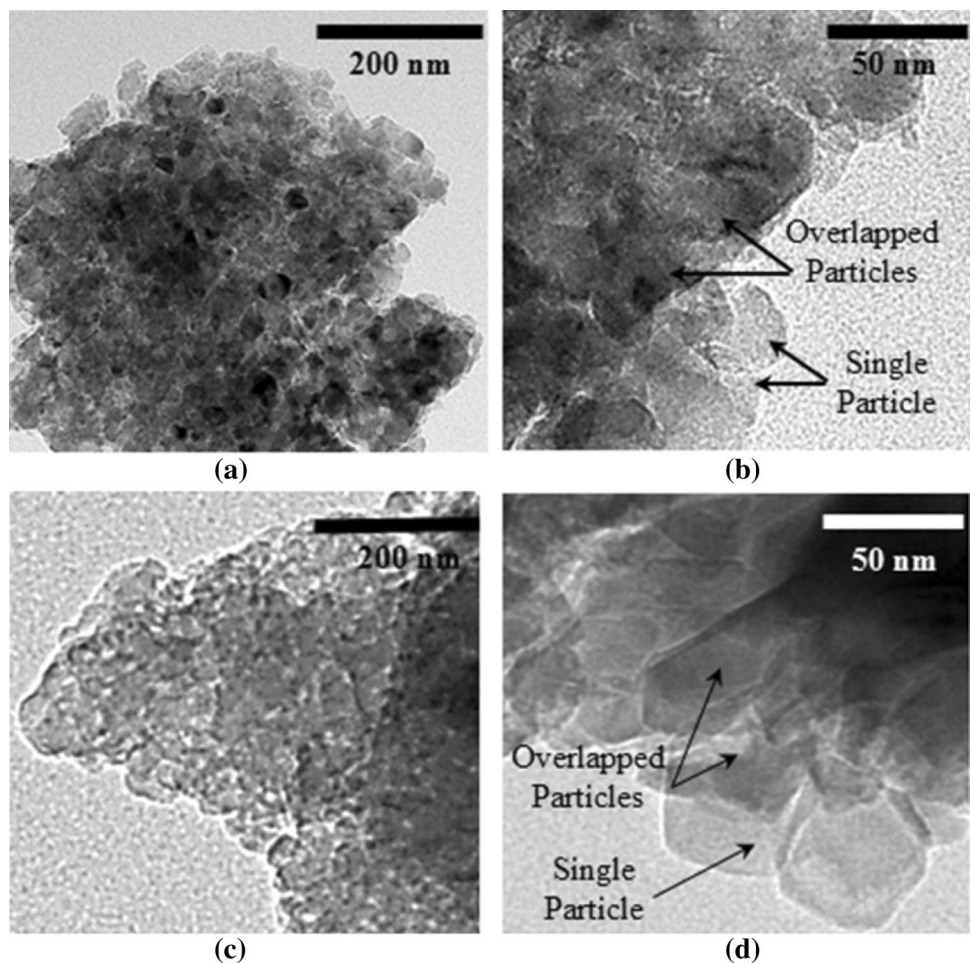


**Fig. 6** TEM images of Cu–TiO<sub>2</sub>/ZnO with Cu = 3 wt% calcined at 500 °C (**a**, **b**) and 700 °C (**c**, **d**)



induced an optical absorption with a steep edge in the visible light region.

It was obvious that the absorption wave length of the new photocatalyst reached between 400 and 800 nm and hence the new photocatalyst was expected to have considerable utilization of visible light for photocatalytic reactions. Besides, the visible light absorption of catalysts at

both calcination temperatures improved by increasing Cu content till 3 wt%. The origin of the visible light sensitivity in Cu-doped TiO<sub>2</sub>/ZnO can be observed by the appearance of additional energy levels by the dopant orbitals (*2p* or *3d*) and oxygen vacancies within the band gaps of TiO<sub>2</sub> and ZnO due to copper doping. The transition of excitation of *3d* electrons from the Cu<sup>2+</sup> ions to the conduction band

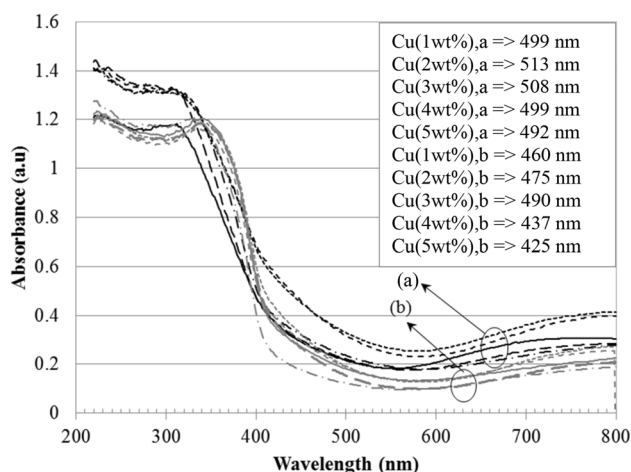


**Fig. 7** The optical absorption curves of Cu–ZnO/TiO<sub>2</sub>, calcined at **a** 500 °C **b** 700 °C, with different copper content of — 1 wt%, ---- 2 wt%, - - - 3 wt%, ——— 4 wt%, —·— 5 wt%

of TiO<sub>2</sub> plays an important role in this lattice. Apart from the Cu orbital levels, oxygen vacancies which are introduced into the lattice of TiO<sub>2</sub>/ZnO by doping enhances the visible light absorption of the lattice. The oxygen vacancy states are at 0.75–1.18 eV below the minimum conduction band of TiO<sub>2</sub> [74]. The band gap narrowing due to the formation of localized states or oxygen vacancies induces the visible-light absorption.

Besides, among the samples, Cu–ZnO/TiO<sub>2</sub> with 2 and 3 wt% Cu concentration showed the largest absorption intensity within the wavelength range of 400–800 nm in both groups of samples. In addition, as shown in Fig. 7, higher absorption intensity and a shift to long wavelength were observed for the samples which were calcined at 500 °C which might be caused by noticeable presence of anatase phase in the photocatalyst lattice since the band gap of anatase (3.2 eV) is wider than that of rutile (3.0 eV).

It should be noted that, the absorption at wavelength of about or less than 380–388 nm is caused by the intrinsic band gap absorption of TiO<sub>2</sub> (depend on its structures equilibrium) [54]. On the other hand, ZnO has an absorption edge at approximately 370–380 nm (band gap 3.35–3.26 eV) [75]. The strong absorption bands at around 400 nm contribute to the excitation of O 2*p* electron to the Ti 3*d* and/or Zn 3*d* level. The large absorption band between 400 and 800 nm is associated to the presence of Cu species. The visible light absorption bands might be due to metallic Cu absorption (225–590 nm), 3-*d* Cu<sup>3+</sup> clusters (400–500 nm) 25, excitation of CuO electron from the valance band to the excitation level (< 730 nm), d–d transition of Cu<sup>2+</sup> (600–800 nm) 25 and Zn<sup>2+</sup> 2*p* clusters (390 to 520 nm).

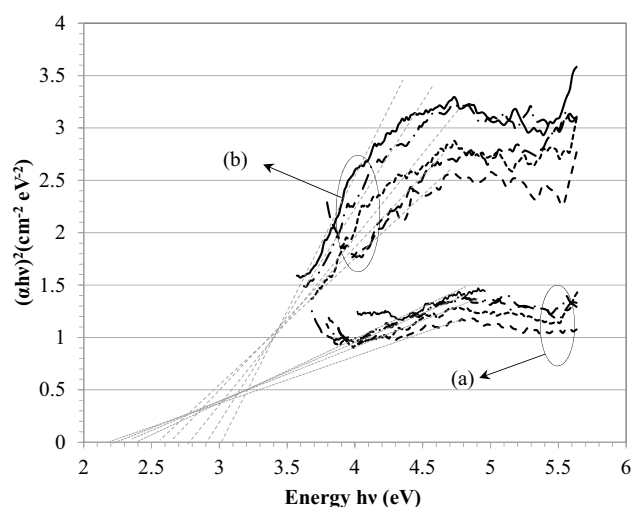


**Fig. 8**  $(\alpha h\nu)^2$  versus energy curve (Kubelka–Munk plots) to estimate the band gap energies of Cu–ZnO/TiO<sub>2</sub> with different copper content and Calcined at (a) 500 °C (b) 700 °C and copper content of — 1 wt%, ---- 2 wt%, - - - 3 wt%, ——— 4 wt%, —·— 5 wt%

### 3.6 Band gap energy level of Cu–ZnO/TiO<sub>2</sub>

In this study, the band gap was approximated through the model presented by Johnson [76]:

$$(Fh\nu)^m = A(h\nu - E_g). \quad (16)$$

In this model,  $F$  is proportional to the absorption coefficient known as Kubelka–Munk value ( $F = (I - R)^2/2R$ ) where  $R$  is the reflectance of the semiconductor.  $A$  and  $E_g$  denote the constant parameter and band gap, respectively.  $m$  represents the type of transition which is equal to 1/2 for direct band gap semiconductor and 2 for indirect band gap semiconductor.  $h\nu$  is calculated by:

$$h\nu = \frac{hc}{\lambda} \quad (17)$$

where,  $h$  is the Planck's constant ( $6.626 \times 10^{-34} \text{ Js}^{-1}$ ) and  $C$  is the speed of light ( $3.0 \times 10^8 \text{ ms}^{-1}$ ). Therefore, band gap is calculated by extrapolating the rising portion of the absorption spectrum to the abscissa at zero absorption. In other words, the intersection between the linear fit and photon energy axis ( $h\nu$ ) gives the value of  $E_g$  (Johnson [76]):

$$A(h\nu - E_g)^m = 0 \Rightarrow h\nu = E_g \quad (18)$$

Eventually, the band gap energy level of the synthesized photocatalysts is presented in Fig. 8. The results are also summarized in Table 2.

Extrapolation of the linear part of the curve to the  $h\nu$ -axis yielded a band gap of about 2.2–2.42 and 2.57–3.02 eV for the samples calcined at 500 and 700 °C, respectively. Undoped TiO<sub>2</sub> and ZnO have the band gap values of 3.2 and 3.37 eV, respectively. It can be suggested that, the band gap of the

**Table 2** Band gap energies of Cu–ZnO/TiO<sub>2</sub> with different copper content and calcined at two different calcination temperatures through Plank's Equation and Kubelka–Munk equation

Model	Kubelka–Munk equation		Plank's Equation	
	500 °C	700 °C	500 °C	700 °C
Calcination temperature				
Cu content (wt%)				
1	2.41	3.02	2.48	2.7
2	2.28	2.65	2.42	2.61
3	2.2	2.57	2.44	2.53
4	2.36	2.77	2.48	2.84
5	2.42	2.91	2.52	2.92

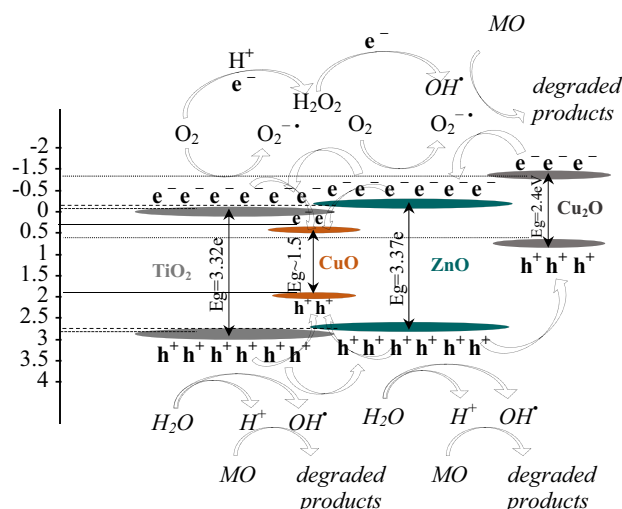
synthesized catalyst in this study was significantly less than that of TiO<sub>2</sub> or ZnO separately. Narrowing of the band gap indicated incorporation of Cu into the lattice of ZnO/TiO<sub>2</sub>. Hence, the band gap decreased, resulting in applicability of visible light in transferring electron between the bands. Furthermore, a significant red shift of 0.21–0.45 eV in the main band gap was observed as the dopant content increased to almost 3 wt% under the temperature of 500 and 700 °C, respectively. More discussion will be presented at the next section (Sect. “The photocatalytic mechanism of Cu–TiO<sub>2</sub>/ZnO under visible light irradiation”).

In the most recent work, Ganesh et al. [77] investigated the Cu-doped TiO<sub>2</sub> (Cu = 0–50 wt%) powders and reported an initial increase in the band-gap energy with increase in copper content in TiO<sub>2</sub> from 0 to 0.1 wt% and then a decrease upon further increase of the dopant content from 0.1 to 10 wt% in both direct and indirect band gap. In another work performed by Sahu and Biswas [78], the authors observed a band-gap energy reduction from 3.3 to 2.51 eV with the increase in Cu-doping concentration in TiO<sub>2</sub> from 0 to 15 wt%.

For calcination at 500 °C, the doped samples exhibited lower band gap energies which originated from either the presence of CuO and Cu<sub>2</sub>O at the surface of the photocatalyst and/or from residual copper due to incomplete pyrolysis. Cupric oxide, CuO possesses 1.4 eV and cuprous oxide, Cu<sub>2</sub>O possesses 2.2 eV. These results, combined with the XRD graphs and morphology pictures, confirmed that the crystallinity of Cu–ZnO/TiO<sub>2</sub> along with its band gap increased at calcination temperatures of 700 °C and above. Band gap increment with calcination temperature in the systems containing TiO<sub>2</sub> and/or ZnO with a metal dopant has also been reported by other authors [79, 80].

To quantitatively estimate the band gap energies (E<sub>g</sub>) and in order to compare the absorption onsets of the Cu–ZnO/TiO<sub>2</sub> samples, Planck's equation was used:

$$E_g = \frac{1240}{\lambda_g} \quad (19)$$

**Fig. 9** Schematic diagram illustrating the charge-transfer process in Cu–TiO<sub>2</sub>/ZnO under simulated solar light irradiation

where,  $\lambda_g$  is the wavelength at the overlap of the vertical and horizontal portions of the spectra. As per Table 2, the band gap estimated by Planck's equation was higher by about 0.3 eV compared to the estimation by Kubelka–Munk's method. However, similar trend was produced by both models.

### 3.7 The photocatalytic mechanism of Cu–TiO<sub>2</sub>/ZnO under visible light irradiation

The possible diagram for charge transfer and energy band positions of Cu–TiO<sub>2</sub>/ZnO is schematically illustrated in Fig. 9. The relevant reactions were already listed in Eqs. (5–11).

Generally, the potential energy level of the conduction and valence band of Cu<sub>2</sub>O lie above than those of TiO<sub>2</sub> and ZnO semiconductors, which assist the transfer of electrons toward valence band of ZnO or TiO<sub>2</sub>. Besides, the potential energy level of the conduction and valence band of both TiO<sub>2</sub> and ZnO semiconductors, are more anodic and more cationic than those of CuO, respectively. This favors transfer of both e<sup>−</sup> and h<sup>+</sup> from TiO<sub>2</sub> and ZnO to CuO, hindering the partial recombination of e<sup>−</sup>/h<sup>+</sup> in the TiO<sub>2</sub> and ZnO. Accordingly, the reactions occurring at the TiO<sub>2</sub>cb, CuOcb and ZnOcb are facilitated.

It should also be noted that, under visible light irradiation, Cu<sub>2</sub>O can reduce O<sub>2</sub> via a multi-electron process and be re-oxidized to CuO [81]. Therefore, although CuO was not detected in XRD analysis, it may be generated under visible light irradiation and so its activity should be considered in photo catalytic reaction. Considering this assumption it can be discussed that, the conduction band of CuO has a more negative potential than required for one-electron oxygen



reduction ( $O_2 + H^+ + e^- \rightarrow HO_2^\circ$ ). Furthermore,  $Cu_2^+$  can react with  $e^-$  (or  $O_2^-$ )  $\rightarrow Cu^+ + (or O_2)$ .  $Cu^+$  can reduce  $O_2$  consuming electrons or be oxidized to  $Cu$ -ions by the photo-generated ZnO or  $TiO_2$  holes to  $Cu_2^+$  [82]. The ZnOvb or  $TiO_2$ vb holes react with the surface  $^-OH$  of the ZnO or  $TiO_2$  releasing OH-radicals. On the other hand, the  $Cu_2Ocb$  lies above the  $ZnO_{cb}$  and  $TiO_{2cb}$ . Accordingly, the excited photoelectrons may be transferred from the  $Cu_2Ocb$  towards the ZnOcb and then to  $TiO_{2cb}$ , whereas the photogenerated holes traverse the opposite direction. In such situation, ZnO as an intermediate stage favors the electron hole transfer between the bands of  $Cu_2O$  and  $TiO_2$  that would considerably reduces the charge recombination rate, increasing the photocatalytic activity of Cu– $TiO_2$ /ZnO.

According to the energy band structure of both  $TiO_2$  and ZnO, the conduction band bottom and the valence band top correspond to mainly Ti/Zn 3d and O 2p states, respectively. The absorption edge of around 380 and 376 nm for un-doped  $TiO_2$  and ZnO results from the band-to-band transition (O 2p  $\rightarrow$  Ti/Zn 3d). In this study, the slight red shift in Cu–ZnO/ $TiO_2$  can be mainly due to sp–d exchange interactions between the band electrons and the localized d-electrons of the  $Cu^{2+}/Cu^{1+}$  substituted titania and/or zinc cations, resulting the formation of O-vacancies with concentration similar to that of added impurities. The sp–d exchange interactions causes an upward shifting of the valence band edge and a rise to downward shifting of the conduction band edge, eventuating a band gap narrowing.

Zuo et al. [83] discussed that the presence of a mini band closely below the conduction band was related to  $O_v$ , associated with  $Ti^{3+}$ , which narrowed the  $TiO_2$  band gap. A similar discussion related to  $O_v$ –induced band gap narrowing was presented by Wang et al. [84] in a system containing ZnO.

Furthermore, as the valance and conduction band of  $TiO_2$  lie below than that of  $Cu_2O$  and ZnO [85, 86], direct transfer of electron from both  $Cu_2Ocb$  and ZnO towards the  $TiO_{2cb}$  in parallel with direct transfer of photogenerated holes from  $TiO_2vb$  to ZnOvb or  $Cu_2Ovb$ , may be the other charge transfer mechanism in Cu– $TiO_2$ /ZnO.

### 3.8 Photocatalytic activity of Cu–ZnO/ $TiO_2$

Figure 10 shows the photocatalytic degradation curves of 300 ml methyl orange 20 ppm with 0.5 g of photocatalyst at different durations. The degradation results were compared to that of pure  $TiO_2$  and  $TiO_2$ /ZnO calcined at 500 °C.

Based on the figure, no significant degradation of MO solution was observed using pure  $TiO_2$  under visible light. Compared to that,  $TiO_2$ /ZnO photocatalyst calcined at 500 °C showed noticeable photodegradation of MO, giving a  $C/C_0$  value of around 0.36 after 150 min under visible light irradiation. However, the figure indicated that Cu–ZnO/ $TiO_2$  could improve the photoactivity of  $TiO_2$ /ZnO, yielding

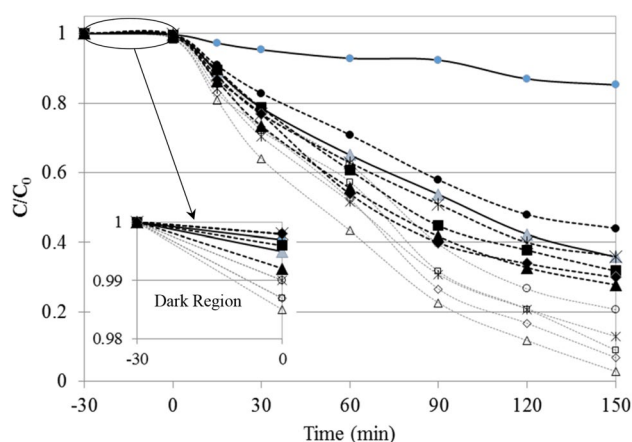


**Fig. 10** Photocatalytic degradation of methylene orange using different Cu–ZnO/ $TiO_2$  with copper concentrations of open square Cu (1 wt%), open diamond Cu (2 wt%), open triangle Cu (3 wt%), times Cu (4 wt%), open circle Cu (5 wt%). Empty bullets calcined at 500 °C, solid bullets calcined at 700 °C, filled circle Pure  $TiO_2$ , filled triangle  $TiO_2$ /ZnO calcined at 500 °C

lower  $C/C_0$  values than that of  $TiO_2$ /ZnO for almost all the reaction durations. As observed, Cu–ZnO/ $TiO_2$  with different Cu contents provided better results, except the one containing 5 wt%, calcined at 700 °C. Totally, the degradation efficiency was higher for the samples calcined at 500 °C compared to that at 700 °C, which should be attributed to the crystal structure of Cu–ZnO/ $TiO_2$  and its band gap energy level. Accordingly, the average final degradation efficiency was around 87% for the former and 64% for the latter. On the other hand, the results clarified that the photocatalytic degradation of the dye increased with copper content up to 3 wt%. After that, the degradation rate reduced noticeably. Therefore, among different photocatalysts, the one with copper content of 3 wt% calcined at 500 °C could reach the maximum degradation of 97% under visible light irradiation.

## 4 Conclusion

In this study, a new hybrid photocatalyst, Cu-doped  $TiO_2$ /ZnO with a Ti to Zn weight ratio of 7:3 and copper content of 1–5 wt% was prepared via sol–gel process, followed by thermal calcinations in air at temperatures of 500 and 700 °C. The prepared photocatalyst powder was characterized in terms of thermal property, crystalline structure, surface morphology, specific surface area, wavelength absorption and band gap energy level. Its photocatalytic performance was then assessed based on photodegradation of methylene orange under visible light irradiation. Compared to the pure  $TiO_2$ /ZnO, the lattice of Cu doped  $TiO_2$ /ZnO was found to be more thermally stable. It was also found that copper dopant delayed the crystalline phase transformation.



Accordingly, anatase was the most dominant phase in the samples calcined at 500 °C and the phase transformation of anatase to rutile was well retarded at calcination temperature of 700 °C. Therefore, higher amount of rutile was formed in samples calcined at 700 °C. The crystalline lattice improved by increasing the dopant content in the photocatalyst matrix and calcination temperature. On the other hand, higher absorption intensity and a shift to long wavelength was markedly observed for the photocatalyst prepared under lower calcination temperature with 3 wt% amount of copper dopant, presenting the lowest band gap values as well; which was about 2.2 and 2.57 eV for the samples calcined at 500 and 700 °C, respectively. Finally, the photocatalysis evaluation revealed an enhanced photocatalytic activity of Cu–ZnO/TiO<sub>2</sub> compared to TiO<sub>2</sub>/ZnO and pure TiO<sub>2</sub> under visible light irradiation. It was noticed that the photoactivity of Cu–ZnO/TiO<sub>2</sub> was significantly influenced by the key operational synthesis factors, i.e. calcination temperature and dopant content. Accordingly, the highest degradation of 97% was obtained by the Cu–ZnO/TiO<sub>2</sub> with 3 wt% copper, calcined at 500 °C.

## References

1. Y. Yao, L. Guan, Y. Ma, M. Yao, J. Mater. Sci. Mater. Electron. **28**, 3013 (2017)
2. H. Gao, Z. Mo, Y. Wang, X. Niu, Z. Li, Mater. Sci. Mater. Electron. **28**, 14543(2017)
3. Y. Liu, D. Zhang, Mater. Sci. Mater. Electron. **28**, 4965 (2017)
4. D. Guerrero-Araque, D. Ramirez-Ortega, R. Gómez, P. Acevedo-Peña, Mater. Sci. Mater. Electron. **28**, 9859 (2017)
5. L. Gurunathan, V. Ponnusamy, Mater. Sci. Mater. Electron. **28**, 18666 (2017)
6. P. Govindhan, C. Pragathiswaran, Mater. Sci. Mater. Electron. **28**, 5063 (2017)
7. M.R.D. Khaki, M.S. Shafeeyan, A.A.A. Raman, W.M.A.W. Daud, Application of doped photocatalysts for organic pollutant degradation—A review. J. Environ. Manage. **198**, 78–94 (2017)
8. O. Aviam, G. Bar-Nes, Y. Zeiri, A. Sivan, Accelerated biodegradation of cement by sulfuroxidizing bacteria as a bioassay for evaluating immobilization of low-level radioactive waste. Appl. Environ. Microbiol. **70**, 6031 (2004)
9. M.L. Krumme, S.A. Boyd, Reductive dechlorination of chlorinated phenols in anaerobic upflow bioreactors. Water Res. **22**, 171–177 (1988)
10. M.R.D. Khaki, M.S. Shafeeyan, A.A.A. Raman, W.M.A.W. Daud, Evaluating the efficiency of nano-sized Cu doped TiO<sub>2</sub>/ZnO photocatalyst under visible light irradiation. J. Mol. Liq. (2017). <https://doi.org/10.1016/j.molliq.2017.11.030>
11. O. Carp, C.L. Huisman, A. Reller, Photoinduced reactivity of titanium dioxide. Prog. Solid State Chem. **32**, 33–177 (2004)
12. A. Fujishima, T.N. Rao, D.A. Tryk, Titanium dioxide photocatalysis. J. Photochem. Photobiol. C **1**, 1–21 (2000)
13. U.I. Gaya, A.H. Abdullah, Heterogeneous photocatalytic degradation of organic contaminants over titanium dioxide: a review of fundamentals, progress and problems. J. Photochem. Photobiol. C **9**, 1–12 (2008)
14. N. Daneshvar, S. Aber, M. Seyed Dorraji, A. Khataee, M. Rasoulifard, Photocatalytic degradation of the insecticide diazinon in the presence of prepared nanocrystalline ZnO powders under irradiation of UV-C light. Separ. Purif. Technol. **58**, 91–98 (2007)
15. S.K. Kansal, M. Singh, D. Sud, Studies on TiO<sub>2</sub>/ZnO photocatalysed degradation of lignin. J. Hazard. Mater. **153**, 412–417 (2008)
16. Y. Abdollahi, A.H. Abdullah, Z. Zainal, N. Yusof, A., Photodegradation of m-cresol by Zinc Oxide under Visible-light. Irrad. Int. J. Chem. **3**, 31–43 (2011)
17. Y. Abdollahi, A.H. Abdullah, Z. Zainal, N.A. Yusof, Photodegradation of o-cresol by ZnO under UV irradiation. J. Am. Sci. **7**, 165–170 (2011)
18. N. Takeda, K. Teranishi, Generation of superoxide anion radical from atmospheric organic matter. Bull. Environ. Cont. Toxicol. **40**, 678–682 (1988)
19. A. Houshmand, W.M.A.W. Daud, M.S. Shafeeyan, Tailoring the surface chemistry of activated carbon by nitric acid: study using response surface method. Bull. Chem. Soc. Jpn. **84**, 1251–1260 (2011)
20. A. Shamiri, M.A. Hussain, F.S. Mjalli, M.S. Shafeeyan, N. Mostoufi, Experimental and modeling analysis of propylene polymerization in a pilot-scale fluidized bed reactor. Ind. Eng. Chem. Res. **53**, 8694–8705 (2014)
21. A.D. Paola, M. Bellardita, L. Palmisano, Brookite, the Least Known TiO<sub>2</sub> Photocatal. Catal. (2013). <https://doi.org/10.3390/catal3010036>
22. J. Ryu, W. Choi, Substrate-specific photocatalytic activities of TiO<sub>2</sub> and multiactivity test for water treatment application. Environ. Sci. Technol. **42**, 294–300 (2007)
23. B. Tryba, M. Toyoda, A.W. Morawski, R. Nonaka, M. Inagaki, Photocatalytic activity and OH radical formation on TiO<sub>2</sub> in the relation to crystallinity. Appl. Catal. B **71**, 163–168 (2007)
24. Y. Du, J. Rabani, The measure of TiO<sub>2</sub> photocatalytic efficiency and the comparison of different photocatalytic titania. J. Phys. Chem. B **107**, 11970–11978 (2003)
25. N. Serpone, G. Sauvé, R. Koch, H. Tahiri, P. Pichat, P. Piccinini, E. Pelizzetti, H. Hidaka, Standardization protocol of process efficiencies and activation parameters in heterogeneous photocatalysis: relative photonic efficiencies  $\zeta_r$ . J. Photochem. Photobiol. A **94**, 191–203 (1996)
26. E.R. Carraway, A.J. Hoffman, M.R. Hoffmann, Photocatalytic oxidation of organic acids on quantum-sized semiconductor colloids. Environ. Sci. Technol. **28**, 786–793 (1994)
27. C. Yogi, K. Kojima, T. Takai, N. Wada, Photocatalytic degradation of methylene blue by Au-deposited TiO<sub>2</sub> film under UV irradiation. J. Mater. Sci. **44**, 821–827 (2009)
28. S.R. Pouran, A. Bayrami, A.A.A. Raman, W.M.A.W. Daud, M.S. Shafeeyan, A. Khataee, Comprehensive study on the influence of molybdenum substitution on characteristics and catalytic performance of magnetite nanoparticles. Res. Chem. Intermed. **44**, 883–900 (2018)
29. S.R. Pouran, M.S. Shafeeyan, A.A.A. Raman, W.M.A.W. Raman, A. Bayrami, Transition metal-substituted magnetite as an innovative adsorbent and heterogeneous catalyst for wastewater treatment, in *Adsorption Processes for Water Treatment and Purification* (Springer, Cham, 2017), pp. 225–247
30. S.R. Pouran, A.A. Aziz, W.M.A.W. Daud, M.S. Shafeeyan, Effects of niobium and molybdenum impregnation on adsorption capacity and Fenton catalytic activity of magnetite. RSC Adv. **5**, 87535–87549 (2015)
31. S.R. Pouran, A. Bayrami, A.A. Aziz, W.M.A.W. Daud, M.S. Shafeeyan, Ultrasound and UV assisted Fenton treatment of recalcitrant wastewaters using transition metal-substituted-magnetite nanoparticles. J. Mol. Liq. **222**, 1076–1084 (2016)
32. S.R. Pouran, A. Bayrami, M.S. Shafeeyan, A.A.A. Raman, W.M.A.W. Daud, A comparative study on a cationic dye removal through homogeneous and heterogeneous Fenton oxidation

- systems. *Acta Chim. Slov.* (2018). <https://doi.org/10.17344/acsi.2017.3732>
33. J.-Y. Park, K.-I. Choi, J.-H. Lee, C.-H. Hwang, D.-Y. Choi, J.-W. Lee, Fabrication and characterization of metal-doped TiO<sub>2</sub> nanofibers for photocatalytic reactions. *Mater. Lett.* **97**, 64–66 (2013)
  34. P. Sangpour, F. Hashemi, A.Z. Moshfegh, Photoenhanced degradation of methylene blue on cosputtered M:TiO<sub>2</sub> (M = Au, Ag, Cu) nanocomposite systems: a comparative study. *J. Phys. Chem. C* **114**, 13955–13961 (2010)
  35. L. Wu, J.C. Yu, X. Fu, Characterization and photocatalytic mechanism of nanosized CdS coupled TiO<sub>2</sub> nanocrystals under visible light irradiation. *J. Mol. Catal. A* **244**, 25–32 (2006)
  36. M.C. Hadj Benhebal, T.S.J. Geens, S.D.L. Ange'lique, Photocatalytic degradation of phenol and benzoic acid using zinc oxide powders prepared by the sol–gel process. *Alexandria Eng. J.* **52**, 517–523 (2013)
  37. Y.-H.H. Chin-Chuan Liu, P.-F. Lai, C.-H. Li, *Dyes Pigm.* **68**, 191e195 (2006)
  38. B.L. Zhu, C.S. Xie, W.Y. Wang, K.J. Huang, J.H. Hu, Improvement in gas sensitivity of ZnO thick film to volatile organic compounds (VOCs) by adding TiO<sub>2</sub>. *Mater. Lett.* **58**, 624–629 (2004)
  39. G. Lakshminarayana, J. Qiu, M.G. Brik, G.A. Kumar, I.V. Kityk, Spectral analysis of Er<sup>3+</sup>-, Er<sup>3+</sup>/Yb<sup>3+</sup>- and Er<sup>3+</sup>/Tm<sup>3+</sup>/Yb<sup>3+</sup>-doped TeO<sub>2</sub>-ZnO-WO<sub>3</sub>-TiO<sub>2</sub>-Na<sub>2</sub>O glasses. *J. Phys.* **20**, 375101 (2008)
  40. Y. Wang, W. Duan, B. Liu, X. Chen, F. Yang, J. Guo, The effects of doping copper and mesoporous structure on photocatalytic properties of TiO<sub>2</sub>. *J. Nanomater.* **2014**, 7 (2014)
  41. C.-S. Kim, J.-W. Shin, Y.-H. Cho, H.-D. Jang, H.-S. Byun, T.-O. Kim, Synthesis and characterization of Cu/N-doped mesoporous TiO<sub>2</sub> visible light photocatalysts. *Appl. Catal. A*, **455** 211–218 (2013)
  42. T.-D. Pham, B.-K. Lee, Cu doped TiO<sub>2</sub>/GF for photocatalytic disinfection of *Escherichia coli* in bioaerosols under visible light irradiation: application and mechanism. *Appl. Surf. Sci.* **296**, 15–23 (2014)
  43. M. Ahmad, E. Ahmed, Z.L. Hong, X.L. Jiao, T. Abbas, N.R. Khalid, B. Part, Enhancement in visible light-responsive photocatalytic activity by embedding Cu-doped ZnO nanoparticles on multi-walled carbon nanotubes. *Appl. Surf. Sci.* **285**, 702–712 (2013)
  44. C. Wu, L. Shen, H. Yu, Y.-C. Zhang, Q. Huang, Solvothermal synthesis of Cu-doped ZnO nanowires with visible light-driven photocatalytic activity. *Mater. Lett.* **74**, 236–238 (2012)
  45. H.R. Pant, B. Pant, R.K. Sharma, A. Amarjargal, H.J. Kim, C.H. Park, L.D. Tijing, C.S. Kim, Antibacterial and photocatalytic properties of Ag/TiO<sub>2</sub>/ZnO nano-flowers prepared by facile one-pot hydrothermal process. *Ceram. Int.* **39**, 1503–1510 (2013)
  46. J. Wang, J. Li, Y. Xie, C. Li, G. Han, L. Zhang, R. Xu, X. Zhang, Investigation on solar photocatalytic degradation of various dyes in the presence of Er<sup>3+</sup>:YAlO<sub>3</sub>/ZnO–TiO<sub>2</sub> composite. *J. Environ. Manage.* **91**, 677–684 (2010)
  47. J. Gao, X. Luan, J. Wang, B. Wang, K. Li, Y. Li, P. Kang, G. Han, Preparation of Er<sup>3+</sup>:YAlO<sub>3</sub>/Fe-doped TiO<sub>2</sub>-ZnO and its application in photocatalytic degradation of dyes under solar light irradiation. *Desalination* **268**, 68–75 (2011)
  48. P. Jongnavakit, P. Amornpitoksuk, S. Suwanboon, N. Ndiege, Preparation and photocatalytic activity of Cu-doped ZnO thin films prepared by the sol–gel method. *Appl. Surf. Sci.* **258**, 8192–8198 (2012)
  49. A. Shamiri, M.S. Shafeeyan, H.C. Tee, C.Y. Leo, M.K. Aroua, N. Aghamohammadi, Absorption of CO<sub>2</sub> into aqueous mixtures of glycerol and monoethanolamine. *J. Nat. Gas Sci. Eng.* **35**, 605–613 (2016)
  50. R. Yusoff, A. Shamiri, M.K. Aroua, A. Ahmady, M.S. Shafeeyan, W.S. Lee, S.L. Lim, S.N.M. Burhanuddin, Physical properties of aqueous mixtures of *N*-methyl-diethanolamine (MDEA) and ionic liquids. *J. Ind. Eng. Chem.* **20**, 3349–3355 (2014)
  51. D. Ramimoghdam, S. Bagheri, S.B. Abd, Hamid, Biotemplated synthesis of anatase titanium dioxide nanoparticles via lignocellulosic waste material. *BioMed Res. Int.* **2014**, 1–7 (2014)
  52. S. Bakardjieva, V. Stengl, L. Szatmary, J. Subrt, J. Lukac, N. Murafa, D. Niznansky, K. Cizek, J. Jirkovsky, N. Petrova, Transformation of brookite-type TiO<sub>2</sub> nanocrystals to rutile: correlation between microstructure and photoactivity. *J. Mater. Chem.* **16**, 1709–1716 (2006)
  53. S. Abedini Khorramia, G. Mahmoudzadeha, S.S. Madania, F. Gharibb, Effect of calcination temperature on the particle sizes of zinc ferrite prepared by a combination of sol–gel auto combustion and ultrasonic irradiation techniques. *J. Ceram. Process. Res.* **12**, 504–508 (2011)
  54. T. Aguilar, J. Navas, R. Alcántara, C. Fernández-Lorenzo, J.J. Gallardo, G. Blanco, J. Martín-Calleja, A route for the synthesis of Cu-doped TiO<sub>2</sub> nanoparticles with a very low band gap. *Chem. Phys. Lett.* **571**, 49–53 (2013)
  55. L. Batistella, L.A. Lerin, P. Brugnerotto, A.J. Danielli, C.M. Trentin, A. Popiolski, H. Treichel, J.V. Oliveira, D. de Oliveira, Ultrasound-assisted lipase-catalyzed transesterification of soybean oil in organic solvent system. *Ultrason. Sonochem.* **19**, 452–458 (2012)
  56. Z. Zhu, M. Hartmann, E.M. Maes, R.S. Czernuszewicz, L. Kevan, Physicochemical characterization of chromium oxides immobilized in mesoporous MeMCM-41 (Me = Al, Ti, and Zr) molecular sieves. *J. Phys. Chem. B* **104**, 4690–4698 (2000)
  57. A. Rahman, M. Ahmed, M. Absi-Halabi, J. Beshara, H. Qabazard, A. Stanislaw, Catalysts in petroleum refining and petrochemical industries, Elsevier, Amsterdam, 1995
  58. B. Jongsomjit, C. Sakdamnusun, J. Goodwin Jr., P. Praserthdam, Co-support compound formation in titania-supported cobalt catalyst. *Catal. Lett.* **94**, 209–215 (2004)
  59. F.C. Gennari, D.M. Pasquevich, Kinetics of the anatase–rutile transformation in TiO<sub>2</sub> in the presence of Fe<sub>2</sub>O<sub>3</sub>. *J. Mater. Sci.* **33**, 1571–1578 (1998)
  60. S. Vemury, S.E. Pratsinis, Dopants in flame synthesis of titania. *J. Am. Ceram. Soc.* **78**, 2984–2992 (1995)
  61. M. Hamadani, A. Reisi-Vanani, A. Majedi, Synthesis, characterization and effect of calcination temperature on phase transformation and photocatalytic activity of Cu, S-codoped TiO<sub>2</sub> nanoparticles. *Appl. Surf. Sci.* **256**, 1837–1844 (2010)
  62. K.V. Baiju, P. Shajesh, W. Wunderlich, P. Mukundan, S.R. Kumar, K.G.K. Warriar, Effect of tantalum addition on anatase phase stability and photoactivity of aqueous sol–gel derived mesoporous titania. *J. Mol. Catal. A*, **276** 41–46 (2007)
  63. M. Hirano, C. Nakahara, K. Ota, M. Inagaki, Direct formation of zirconia-doped titania with stable anatase-type structure by thermal hydrolysis. *J. Am. Ceram. Soc.* **85**, 1333–1335 (2002)
  64. K.S.V.D. Binas, T. Maggos, A. Katsanaki, G. Kiriakidis, Synthesis and photocatalytic activity of Mn-doped TiO<sub>2</sub> nanostructured powders under UV and visible light. *Appl. Catal. B* **113–114**, 79–86 (2012)
  65. M.S. Shafeeyan, A. Houshmand, A. Arami-Niya, H. Razaghi-zadeh, W.M.A.W. Daud, Modification of activated carbon using nitration followed by reduction for carbon dioxide capture. *Bull. Korean Chem. Soc.* **36**, 533–538 (2015)
  66. A. Houshmand, M.S. Shafeeyan, A. Arami-Niya, W.M.A.W. Daud, Anchoring a halogenated amine on the surface of a microporous activated carbon for carbon dioxide capture. *J. Taiwan Inst. Chem. Eng.* **44**, 774–779 (2013)
  67. D.R. Sahu, L.Y. Hong, S.-C. Wang, J.-L. Huang, Synthesis, analysis and characterization of ordered mesoporous TiO<sub>2</sub>/SBA-15

- matrix: effect of calcination temperature. *Microp. Mesopor. Mater.* **117**, 640–649 (2009)
68. M. Hamadani, A. Reisi-Vanani, A. Majedi, Preparation and characterization of S-doped TiO<sub>2</sub> nanoparticles, effect of calcination temperature and evaluation of photocatalytic activity. *Mater. Chem. Phys.* **116**, 376–382 (2009)
  69. J. Shi, S. Chen, S. Wang, Z. Ye, P. Wu, B. Xu, Favorable recycling photocatalyst TiO<sub>2</sub>/CFA: Effects of calcination temperature on the structural property and photocatalytic activity. *J. Mol. Catal. A* **330**, 41–48 (2010)
  70. Y.U. Ahn, E.J. Kim, H.T. Kim, S.H. Hahn, Variation of structural and optical properties of sol–gel TiO<sub>2</sub> thin films with catalyst concentration and calcination temperature. *Mater. Lett.* **57**, 4660–4666 (2003)
  71. S.N.R. Inturi, T. Boningari, M. Suidan, P.G. Smirniotis, Visible-light-induced photodegradation of gas phase acetonitrile using aerosol-made transition metal (V, Cr, Fe, Co, Mn, Mo, Ni, Cu, Y, Ce, and Zr) doped TiO<sub>2</sub>. *Appl. Catal. B* **144**, 333–342 (2014)
  72. G. Marci, V. Augugliaro, M.J. López-Muñoz, C. Martín, L. Palmisano, V. Rives, M. Schiavello, R.J.D. Tilley, A.M. Venezia, Preparation characterization and photocatalytic activity of polycrystalline ZnO/TiO<sub>2</sub> systems. 1. surface and bulk characterization. *J. Phys. Chem. B* **105**, 1026–1032 (2001)
  73. C.-J. Lin, W.-T. Yang, Ordered mesostructured Cu-doped TiO<sub>2</sub> spheres as active visiblelight- driven photocatalysts for degradation of paracetamol. *Chem. Eng. J.* **237**, 131–137 (2014)
  74. D.C. Cronemeyer, Infrared absorption of reduced rutile TiO<sub>2</sub> single crystals. *Phys. Rev.* **113**, 1222–1226 (1959)
  75. R.C. Pawar, D.-H. Choi, J.-S. Lee, C.S. Lee, Formation of polar surfaces in microstructured ZnO by doping with Cu and applications in photocatalysis using visible light. *Mater. Chem. Phys.* **151**, 167–180 (2015)
  76. E.J. Johnson, Absorption near the fundamental edge. *Semicond. Semimetals* **3**, 153–258 (1967)
  77. P.P. Ganesh, I. Kumar, J.M. Annapoorna, M. Sumliner, N.Y. Ramakrishna, G. Hebalkar, G. Padmanabham, Sundararajan, Preparation and characterization of Cu-doped TiO<sub>2</sub> materials for electrochemical, photoelectrochemical, and photocatalytic application. *Appl. Surf. Sci.* **293**, 229–247 (2014)
  78. M. Sahu, P. Biswas, Single-step processing of copper-doped titania nanomaterials in a flame aerosol reactor. *Nanoscale Res. Lett.* **6**, 441–441 (2011)
  79. M.H. Habibi, N. Talebian, J.-H. Choi, The effect of annealing on photocatalytic properties of nanostructured titanium dioxide thin films. *Dyes Pigm.* **73**, 103–110 (2007)
  80. C. Yang, H. Fan, Y. Xi, J. Chen, Z. Li, Effects of depositing temperatures on structure and optical properties of TiO<sub>2</sub> film deposited by ion beam assisted electron beam evaporation. *Appl. Surf. Sci.* **254**, 2685–2689 (2008)
  81. A.J. Nozik, Photoelectrochemistry: applications to solar energy conversion. *Annu. Rev. Phys. Chem.* **29**, 189–222 (1978)
  82. J. Bandara, I. Guasaquillo, P. Bowen, L. Soare, W.F. Jardim, J. Kiwi, Photocatalytic storing of O<sub>2</sub> as H<sub>2</sub>O<sub>2</sub> mediated by high surface area CuO. Evidence for a reductive-oxidative interfacial mechanism. *Langmuir*. **21**, 8554–8559 (2005)
  83. F. Zuo, L. Wang, T. Wu, Z. Zhang, D. Borchardt, P. Feng, Self-doped Ti<sup>3+</sup> enhanced photocatalyst for hydrogen production under visible light. *J. Am. Chem. Soc.* **132**, 11856–11857 (2010)
  84. J. Wang, Z. Wang, B. Huang, Y. Ma, Y. Liu, X. Qin, X. Zhang, Y. Dai, Oxygen vacancy induced band-gap narrowing and enhanced visible light photocatalytic activity of ZnO. *ACS Appl. Mater. Interfaces*. **4**, 4024–4030 (2012)
  85. P. Zhou, J. Yu, M. Jaroniec, All-solid-state Z-scheme photocatalytic systems. *Adv. Mater.* **26**, 4920–4935 (2014)
  86. J. Yu, J. Low, W. Xiao, P. Zhou, M. Jaroniec, Enhanced photocatalytic CO<sub>2</sub>-reduction activity of anatase TiO<sub>2</sub> by Coexposed {001} and {101} facets. *J. Am. Chem. Soc.* **136**, 8839–8842 (2014)